Postprint of: Doroszko M., Falkowska A., Seweryn A., Image-based numerical modeling of the tensile deformation behavior and mechanical properties of additive manufactured Ti–6Al–4V diamond lattice structures, MATERIALS SCIENCE AND ENGINEERING A-STRUCTURAL MATERIALS PROPERTIES MICROSTRUCTURE AND PROCESSING, Vol. 818 (2021), 141362, DOI: 10.1016/j.msea.2021.141362

Image-based numerical modeling of the tensile deformation behavior and mechanical properties of additive manufactured Ti-6Al-4V diamond lattice structures

M. Doroszko [a,*], A. Falkowska [a], A. Seweryn [b]

m.doroszko@pb.edu.pl, a.falkowska@pb.edu.pl, a.seweryn@pb.edu.pl

[a] Department of Mechanics and Applied Computer Science, Faculty of Mechanical Engineering, Bialystok University of Technology, 45C Wiejska, Bialystok 15-351, Poland

[b] Institute of Ocean Engineering and Ship Technology, Faculty of Mechanical Engineering and Ship Technology, Gdańsk University of Technology, 11/12 Gabriela Narutowicza, Gdańsk, 80-233, Poland

Keywords: deformation process, finite element analysis, additive manufacturing, lattice structures, microtomography

ABSTRACT

This work concerns the numerical modeling of the deformation process and mechanical properties of structures obtained by the additive method laser power bed fusion (LPBF). The investigation uses diamond structures of Ti-6Al-4V titanium implantation alloy with various relative densities. To model the process of tensile deformation of the materials, geometric models were used, mapping the realistic shape of the examined structures. To recreate the geometry of the samples, computed tomography (CT) and microtomography (micro-CT) were used, which allowed to obtain two accuracy levels of the mapping details of the investigated structures shape. Taking into account the nonlinearity of the material in the computational model makes it possible to model the deformation process of cellular materials until the fracture initiation. On the basis of the performed calculations using the finite element method (FEM), the stress and strain distributions in deformed structures were obtained and analyzed. The relationship between the shape of cellular structures and their effective mechanical properties on a macroscopic scale was investigated. The influence of the accuracy of the structures shape mapping on their strength properties and stress and strain distributions was also described. On the basis of the conducted research, fracture initiation localizations in titanium cellular structures were indicated. Finally, the results of the numerical calculations were verified by experimental tests.

1. INTRODUCTION

The intensive development of orthopedic implants over the last decades has forced increased efforts in the field of designing new implant constructions. The significant development of additive

technologies has contributed greatly to this. It makes possible to produce any porous structures with mechanical properties similar to those of bone tissue [1–4].

The use of 3D printing for biomedical applications enables the production of implants from materials distinguished by high biocompatibility. These criteria are met by titanium alloys such as Ti-6Al-4V, which apart from this feature are also characterized by high strength with a low value of elasticity modulus. Moreover, elements made of titanium alloys are lighter than those of other metals (eg 316L steel) and have a higher corrosion resistance [5,6]. One of the popular methods of 3D printing is laser power bed fusion (LPBF) according to ASTM [7], also known as selective laser melting (SLM). It consists in spreading successive layers of the powder of the created element, and then the action of a laser with a specific power, melts the powder particles into a compact whole. This method enables the production of whole elements with a specific structure, and thus with a defined relative density [8–10].

Conducting experimental tests of porous materials requires the development of an appropriate methodology, starting from the design of specimens and holders of the testing machine to determining the load conditions and conducting advanced microstructure studies [11–15]. The strength tests of materials obtained by laser melting, mainly the type of structure [16,17], and the degree of material densification are taken into account [18–21]. Obtaining optimal strength properties may result in the fact that the tested material will have a high similarity to the properties of bone tissue [18,22].

Modeling the deformation process and mechanical properties of materials, taking into account their structure on a mesoscopic scale, is currently the subject of many scientific works. The study of Askari et al. [23] presents micro-CT based finite element modeling of the compressive properties of zirconia foam scaffolds for bone tissue engineering. Doroszko and Seweryn [24] describes the developed procedure and results of large deformation compressive behavior of porous 316L sinters using microtomography. In the work of Legwand et al. [25], the communication mechanism between microscale and macroscale models of the multiscale numerical approach was investigated. The works Zhou and Zhou [26,27] concern computed tomography based numerical investigation of strength the properties of sintered iron ore. For numerical modeling of the mechanical properties of cellular materials, geometric models are often used to simplify the real shape of structures on a mesoscopic scale. In the works of Baranowski et al. [28] and Kucewicz et al. [29], the compressive deformation and failure of honeycomb structures were modeling. The work of Geng et al. [30] concerns the numerical modeling of three-dimensional lattice structures fracture under quasi-static tensile load. Drücker et al. [31] describe the mechanical characterization of additively manufactured Ti-6Al-4V lattice structures considering progressive damage. In the work of Wang et al. [32], the compressive behavior of modified gyroid structures with bone-like mechanical properties was analysed. Due to the complex spatial shape of structures, various approaches are used to take into account the real shape of material discontinuities in numerical modeling [33–35]. Computer simulations using realistic geometric models enable a better understanding and a more detailed description of the deformation

and fracture process of materials with a complex three-dimensional mesoscopic structure [36–38]. For the detailed mapping of the realistic shape of lattice structures in numerical modeling, the most commonly used approaches are based on the use of computed microtomography. In the work of Amani et al. [39], the compression behavior of lattice structures produced by selective laser melting was modeled using computed tomography. The article by Boniotti et al. [40] presents the numerical investigation of the compressive fatigue strength of lattice structures of AlSi7Mg. The study of Hazeli et al. [41] presents a relationship between manufacturing variables on the porosity distribution, quasi-static, and dynamic behavior of additively manufactured lattice structures (AMLS) using micro-CT. In the work of Galarreta et al. [42], the procedure for evaluation the mechanical properties of porous structures was described. Including the imperfections of individual struts and lattice structure nodes in the calculations allows for a more accurate simulation of the material deformation process than in the case of highly simplified models. In the work of Dallago et al. [43], the effect of geometrical defects and residual stresses on the elastic modulus and fatigue resistance of cellular specimens was investigated. Lei et al. [44] present the evaluation of compressive properties and struts imperfections of multilayer lattice structures by finite element analysis. The article of Lozanovski et al. [45] describes the generation of manufacturing defects in computational models of additively manufactured lattice structures to improve simulation accuracy. In the work of Xiao et al. [46], the geometric defects influence of octet truss and rhombic dodecahedron lattice fabricated by electron beam melting on compressive deformation was studied. In the article of Yanez et al. [47], the surface roughness effects on the fatigue behavior of gyroid cellular Ti-6Al-4V structures obtained by additive manufacturing were investigated.

This paper describes the modeling of the deformation process and the mechanical properties of the tensile cellular structures (under quasi-static conditions) of the Ti-6Al-4V alloy, taking into account the shape of imperfections resulting from the production process. Diamond lattice structures with different relative densities were analyzed [15]. In order to take into account the shape of structures and their imperfections in numerical calculations, techniques using x-rays: computed tomography and microtomography were used. Due to the characteristics and accuracy of both measurement techniques used, models with two levels of mapping, the geometric details of the investigated lattice structures were obtained. The study investigated the influence of the accuracy of the structure geometry mapping, in particular the imperfections occurring in the structures, on the process of their deformation and the values of effective mechanical properties. The differences in the deformation process of diamond lattice structures resulting from the different relative density of the material were also described. The influence of the material's relative density on the location of the stress concentration in deformed structures was determined. The stress and strain distributions in the investigated structures at the moment of fracture initiation in the material were also analyzed. Finally, the results of the numerical calculations were verified using the results of experimental studies.

2. MATERIALS AND EXPERIMENTAL TESTS

In this study, Ti-6Al-4V titanium alloy used mainly as a biomedical material for the production of various types of implants (including bone replacement elements) due to its high biocompatibility [9] and appropriate strength properties was used. The material for the production of the specimens was LaserForm Ti Gr23 powder (3D Systems) with a particle size from several up to 40 μm. In Table 1 shown the chemical composition of the used Ti-6Al-4V powder. For the tests, diamond lattice structures with nominal relative density of 18.5%, 27%, 50%, and 66% (Fig. 1) and strut thicknesses of 0.49, 0.6, 0.7, and 1.2 mm respectively were produced. This corresponds to porosity values of 81.5%, 73%, 50%, and 34% respectively. The relative density ρ_{rel} was defined as the ratio of the density of the sample with the cellular structure ρ_{cell} to the density of the solid specimen ρ_s obtained by the additive manufacturing technique $\rho_{rel} = \rho_{cell}/\rho_s$. Specimens were obtained by the laser power bed fusion additive method. The main parameters of sample production using LPBF are layer thickness 60 μm and scanning speed 400 mm/s. The remaining parameters were optimized by the material manufacturer, Medgal® Orthopeadic Implants & Instruments, based on the work of Benedetti et al. [48]. To remove the residual stresses resulting from the 3D printing process, the specimens were heated in a vacuum furnace at 920°C. More details on the investigated materials are described in the work of Falkowska et al. [15].

Table 1. Chemical composition of Ti-6Al-4V powder [%] used for the production of diamond lattice structures.

Material	C	Fe	H	N	O	V	Y	Other
Ti-6Al-4V	≤0.08	≤0.25	≤0.12	≤0.03	≤0.13	3.5-4.5	≤0.005	≤0.40

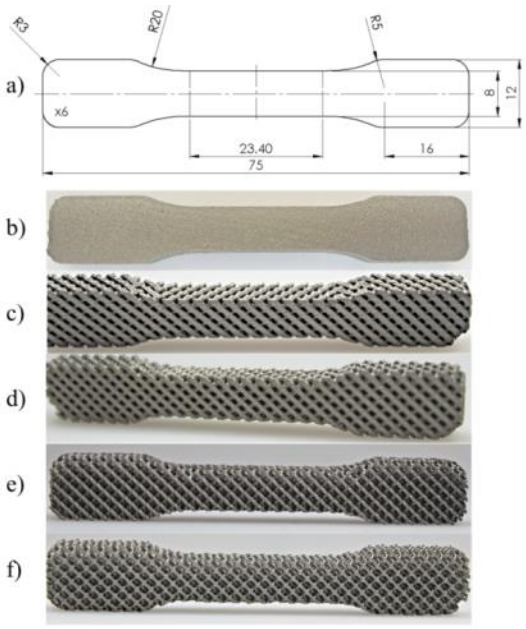

Fig. 1. Tested materials obtained by the LPBF method: a) specimen dimensions and specimens with different relative density values b) near to 1 (solid material), b) 66%, c) 50%, d) 27% and e) 18.5%.

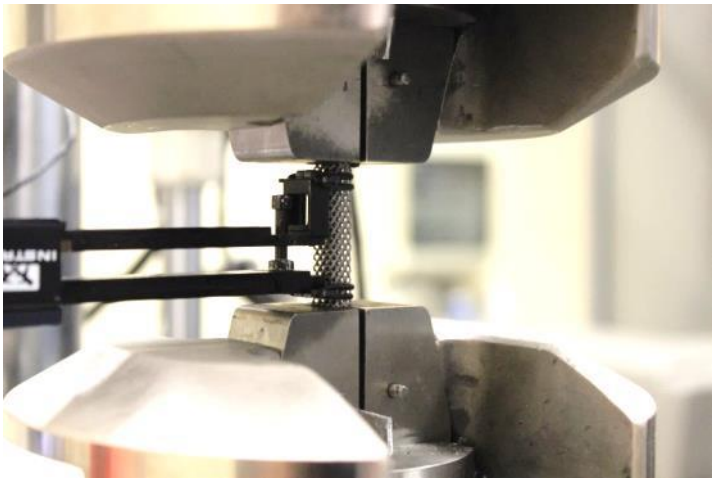

Fig. 2. A specimen of a diamond structure with an extensometer prepared for a monotonic tensile test.

The monotonic tensile test was carried out on the MTS 858 Mini Bionix testing machine with digital FlexTest SE control. The change in the gauge length was recorded using an Instron 2620-201 extensometer with a gauge length of 25 mm and a range of ± 5 mm (Fig. 2). The load was applied at a speed of 0.01 mm/s, while the data was recorded at a frequency of 25 Hz. On the basis of the monotonic tensile test, the effective tensile curves (based on three specimens for each relative density) were determined (Fig. 3) and the most important effective strength properties for Ti-6Al-4V titanium alloys with various degrees of diamond structure densification and solid specimens (Table 2), such as: Young's modulus E_{eff}, Poisson's ratio ν_{eff}, yield stress $\sigma_{0.2\text{eff}}$, ultimate tensile strength $\sigma_{\text{eff}}^{\max}$, and relative elongation A_{eff}. The effective values refer to and are usually used to describe the averaged values of stresses and strains in inhomogeneous materials such as porous materials, foams, composites. When determining the effective values, it is assumed that the material is solid and homogeneous, that is, voids in the form of pores are not taken into account when defining the cross-section needed to calculate the effective stress. On the other hand, the effective deformation determines the macroscopic deformation of the material taking into account only the change in the length of the measurement base. The effective stress σ_{eff} was calculated as F/A_0, where F is the reaction force and A_0 is the initial cross-sectional area of the specimen. The effective strain ε_{eff} was defined as $\Delta l/l_0$, where Δl is the change in the gauge length and l_0 is the initial length of the analysed gauge length. The strength properties obtained from these stress and strain values are often called effective [49–51]. The nominal stress and strain values are calculated in a similar way, while the nominal values are usually used for conventional solid materials. It can be seen that despite the difference in the relative density values in individual specimens, a similar value of the maximum effective strain was obtained for almost tested materials (Fig. 3).

The tensile test of Ti-6Al-4V near to solid specimens was carried out in the same experimental conditions as the tests of lattice structures described above.

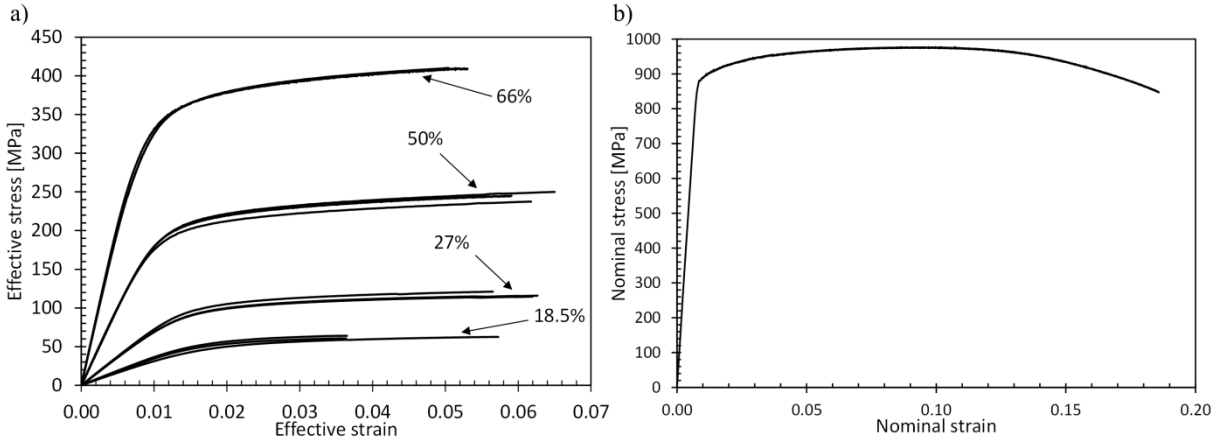

Fig. 3. Nominal and effective stress-strain relationship during monotonic tension of specimens made of Ti-6Al-4V titanium alloy by LPBF: a) with different relative density and b) solid specimens.

Table. 2. Effective strength properties of Ti-6Al-4V lattice structures with various relative densities, produced by the LPBF.

No.	ρ_{rel} [%]	E_{eff} [GPa]		ν_{eff}	$\sigma_{0.2eff}$ [MPa]		σ_{eff}^{max} [MPa]		A_{eff} [%]
1		3.8			44.1		66.7		
2	18.5	3.6	3.7	0.42	40.3	42.4	59.3	62.5	5.7
3		3.7			42.8		61.5		
4		7.3			86.2		109.5		
5	27	7.3	7.4	0.35	87.4	89.2	113.7	117.2	5.7
6		7.5			94.0		128.4		
7		19.9			191.1		238.5		
8	50	20.6	20.4	0.32	194.3	193.5	245.7	244.2	6.1
9		20.6			195.1		248.4		
10		41.3			291.8		405.5		
11	66	42.8	41.8	0.31	315.7	300.8	416.7	410.0	5.2
12		41.3			294.9		407.8		

To determine the fracture locations in the tensile diamond structures, microscopic investigation was performed using the optical Digital Microscope Olympus DSX110 device (Fig. 4). In the tested materials, fracture occurs in the struts near the nodes of the structure, although there are also cases where the fracture occurs at a certain distance from the node. For a structure with a relative density of 18.5%, the fracture surfaces are at various distances from the structure nodes. However, for the relative density of 27%, a small part of them is distant from the nodes. The shape of the cellular

structures of materials with a higher value of the relative density of 50% and 66% (and a greater thickness of the struts) determines the fracture of the struts near the structure nodes.

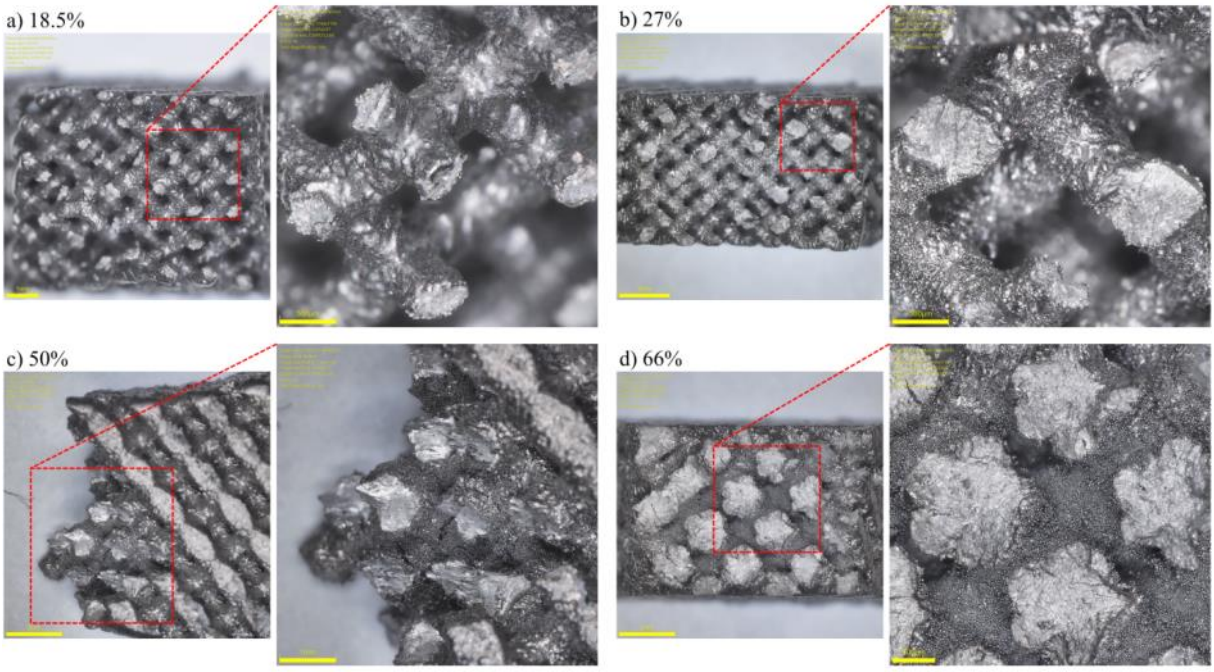

Fig. 4. Fracture surfaces of the tested cellular diamond structures with relative density: a) 18.5%, b) 27%, c) 50%, and d) 66%.

3. NUMERICAL MODELING

This paper presents a procedure for numerical modeling of quasi-static tension of diamond lattice structures. It was also described how the deformation process of the material is influenced by the imperfections of mapping the real shape of titanium cellular structures obtained by means of additive manufacturing (LPBF).

3.1. Determination of a solid material nonlinearity

To determine the material nonlinearity of the tensile cellular structures, experimental tensile tests of the solid Ti-6Al-4V material obtained under the same production conditions as the tested cellular structures were also carried out. A microtomographic examination of the obtained almost solid material under study was also performed. The microporosity of the tested sample was 0.00564%. Due to the negligible porosity created in the solid material (as a result of laser melting of powder particles), it has a negligible impact on the deformation process on a macro scale. It is also noticeable after analyzing the obtained values of Young's modulus, yield stress and strain-stress curves, which are similar to those obtained for Ti-6Al-4V solid alloy produced by methods other than additive manufacturing. For this reason, it was assumed for the numerical modeling that there are no voids in the solid specimens.

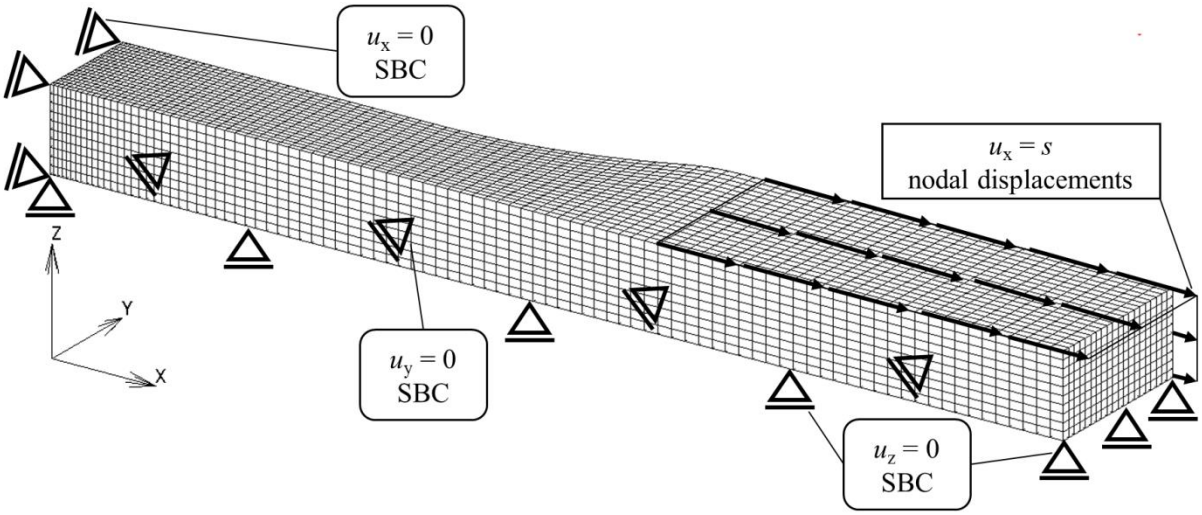

Fig. 5. Boundary conditions and finite element mesh used for tension modeling of a specimen made of solid Ti-6Al-4V material.

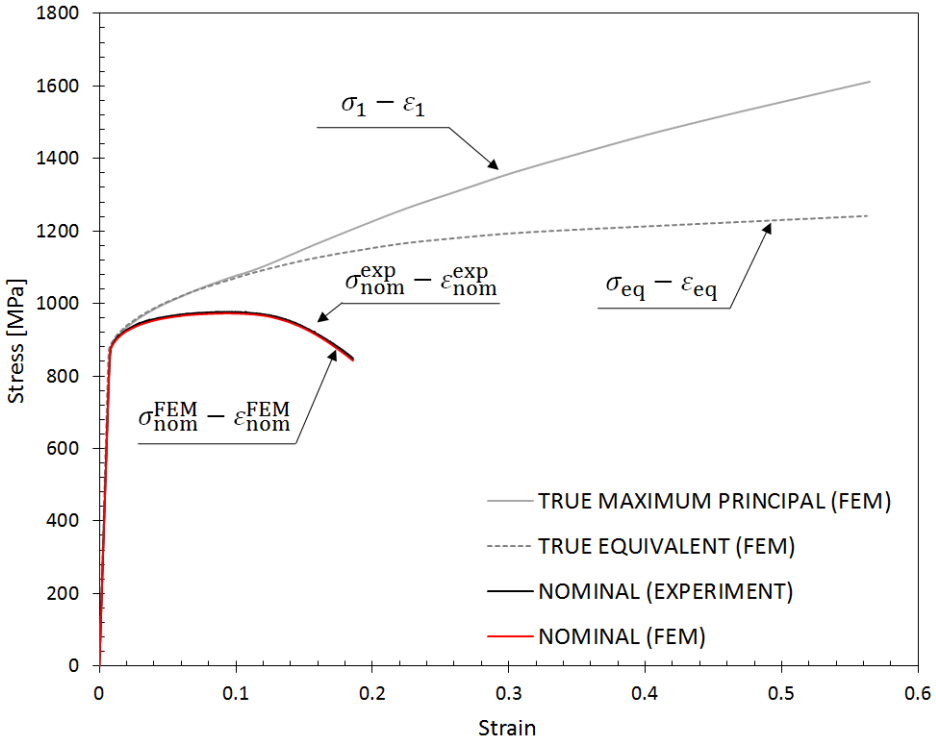

Fig. 6. Comparison of the true and nominal stress-strain relationship obtained by means of numerical calculations and experimental tests.

A hybrid experimental-numerical method was used to determine the nonlinearity of the material [52,53]. For this purpose, experimental studies and tensile calculations for solid Ti-6Al-4V material were carried out using the MSC.Marc software based on the finite element method. A three-dimensional geometric model representing a quarter of the entire geometry of the tested

specimens was used for numerical calculations. The model was divided into 18 400 solid 8-node isoparametric finite elements with linear interpolation of the Hex 7 type [54]. The finite element mesh was densified towards the center of the specimen. Symmetric boundary conditions (SBC) were used in the calculations by assigning zero displacements of the finite element nodes lying on the three planes of the geometric model constituting the symmetry planes of the sample (Fig. 5). Tensile modeling of the finite element mesh was obtained by assigning nodal displacements in the direction of positive x-axis values for nodes located on the significant surfaces of gripping part, in a similar way to the experimental studies. For the calculations, the elastic-plastic model of the material with hardening was used. Values of Young's modulus E_s = 116.9 GPa and Poisson's ratio ν_s = 0.31 obtained by experimental tests were used [15]. Material yielding was determined using the Huber-von Mises criterion and the nonlinearity in the range of plastic strains using the true stress-plastic strain curve. The true tensile curve of the Ti-6Al-4V alloy was determined iteratively. Initially, the nominal stress-strain curve obtained from the experimental tests was used as the nonlinearity of the material in the numerical calculations. The values of stress σ_{nom} and strain ε_{nom} were assumed as nominal values (Fig. 6), not taking into account the changes in the cross-sectional area and the length of the initial measurement base. After the calculations, the convergence of the nominal curves obtained numerically and experimentally was checked, and then the true hardening curve was modified to improve their convergence. The iterations described above were repeated until the satisfactory compliance of the nominal stress-strain curves obtained by calculations and experiment. Then, the true stress-plastic strain curve (Fig. 8) was obtained at the center point of the specimen, i.e. at the point where the maximum values of stress and plastic strain are located (Fig. 7). The use of nonlinearity obtained by the experimental-numerical method allows to take into account the change in the cross-sectional area and the stress distribution in the most plastically deformed localization of the specimen (Fig. 7). Fig. 6 also shows the convergence of the nominal stress-strain curves obtained by numerical calculation and experiment.

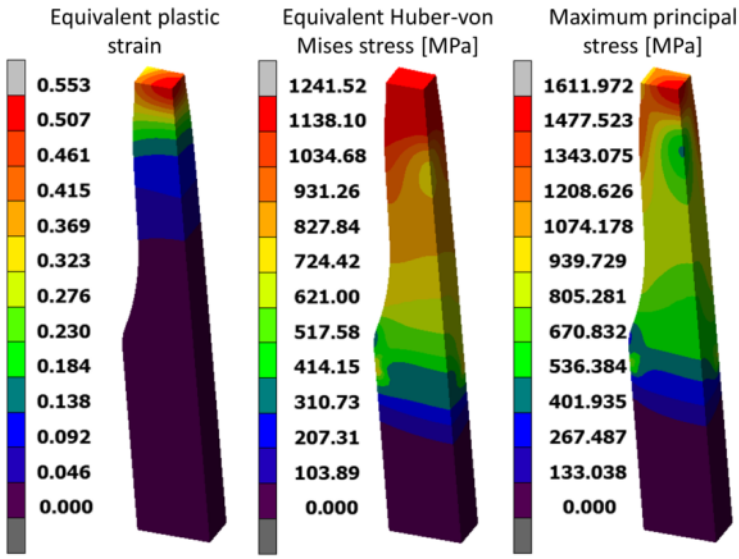

Fig. 7. Distributions of plastic strain and stress in a solid Ti-6Al-4V specimen at the moment of material fracture initiation.

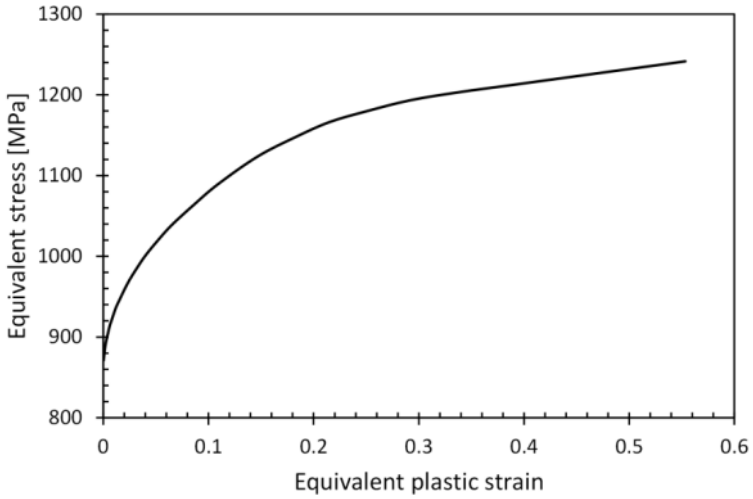

Fig. 8. The true equivalent stress-equivalent plastic strain curve for Ti-6Al-4V solid material obtained by 3D printing.

3.2. Recreating the shape of lattice structures using tomographic techniques

In the numerical modeling of stress and strain fields of the tensile process described in the paper, the realistic shape of spatial diamond structures was taken into account. For this purpose, two tomographic devices were used. As a result, geometric models of lattice structures were obtained, mapping the details of the geometry of the produced specimens with varying accuracy. As a result, geometric models with two accuracy levels were obtained in order to describe the influence of micro and macrodefects on the deformation process of the lattice structures.

To study the influence of macroscopic imperfections of the lattice structure on its mechanical behavior, a Nikon XT H 225 CT was used. In the studies with the use of computed tomography, whole specimens of the tested materials were used. The following scanning parameters were used for CT measurements: pixel size of 127 μm, source voltage of 170 kV, and current of 341 μA. From a part of the gauge length of the specimens, 1 geometric model was separated for each of the investigated structures. Cuboidal models with dimensions of 6 × 8 × 2.5 mm were obtained (Fig. 9). However, in order to take into account the microscopic imperfections of the structures, the Bruker SkyScan 1172 micro-CT was used. The following measurement parameters were used for microtomographic investigation: pixel size of 2.94 μm, source voltage of 100 kV, and current of 100 μA. In the case of micro-CT measurements, the specimens dimensions have been decreased due to the device characteristics. From the gauge length, specimens with a cross-section equal to a quarter of the cross-sectional area (3 × 4 mm) of the whole produced samples were cut. Based on the obtained images,

diamond structures were recreated in the form of geometric models with dimensions of 3 × 4 × 2.5 mm (Fig. 10).

An important aspect influencing the mapping of the geometry of diamond structures was the tomographic image thresholding procedure. Initially, a median filter was applied to the obtained CT images reconstruction in order to remove noise types such: Gaussian, random and salt and pepper noises. This filter to remove the noise pixels on the protein crystal images before binarization operation. In order to binarize, the automatic thresholding method presented by Otsu [55] was used. The method is based on the Otsu criterion. It is a nonparametric and unsupervised method of automatic threshold selection for image segmentation. The procedure is very simple, utilizing only the zeroth- and the first-order cumulative moments of the gray-level histogram.

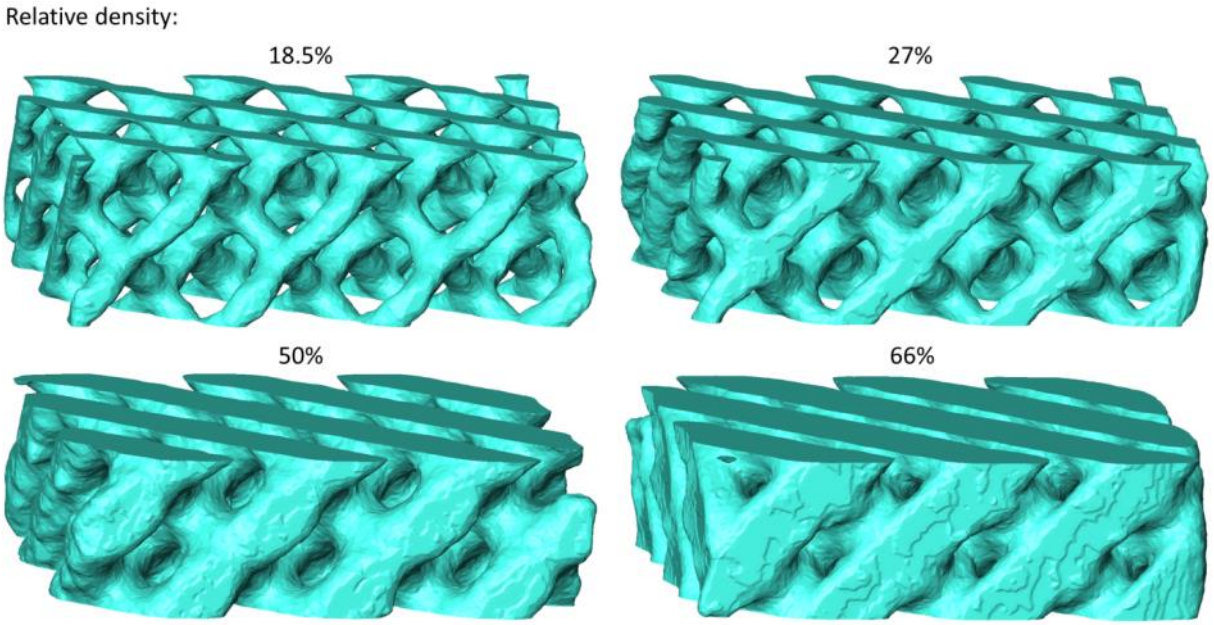

Fig. 9. Geometric models obtained on the basis of computed tomography.

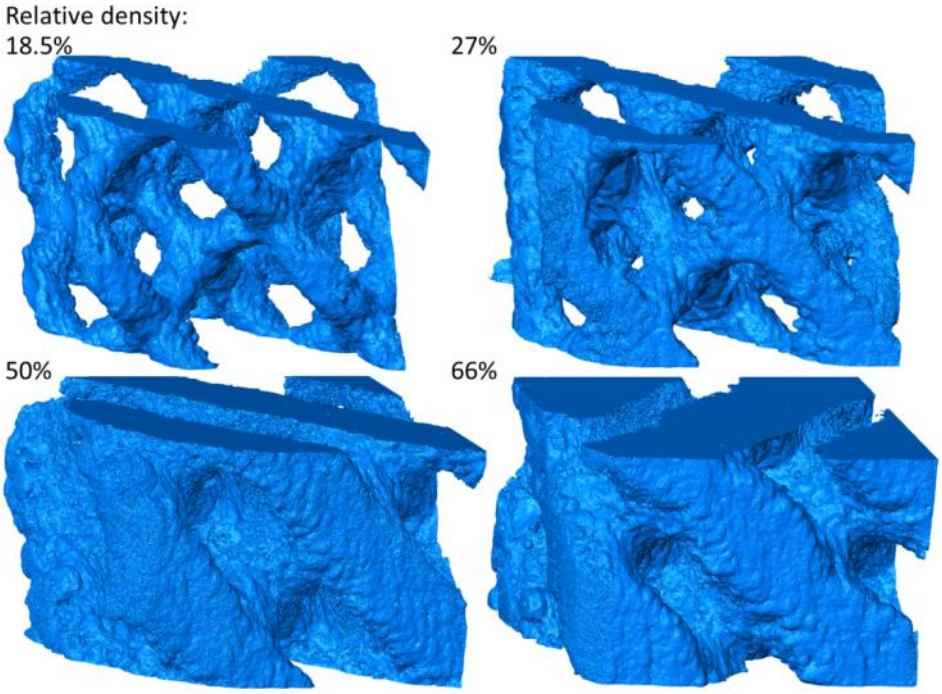

Fig. 10. Geometric models obtained on the basis of computed microtomography.

The accuracy of the measurement with the CT device allowed for the mapping of the structure topology as well as the waviness and thickness of the struts. The greater accuracy of the micro-CT device (pixel size 2.94 μm) in relation to CT (pixel size 127 μm) made it possible to recreate a much larger number of geometric details of the tested cellular structures. These include imperfections on the surface such as micronotches caused by the manufacturing process and powder particles that have not been completely fused into the structure. Micro-CT measurements also allowed taking into account the micropores inside the struts and the structures nodes (Fig. 11). Geometric models from CT and micro-CT images were generated using Thermo Scientific Avizo 9.7.0 software.

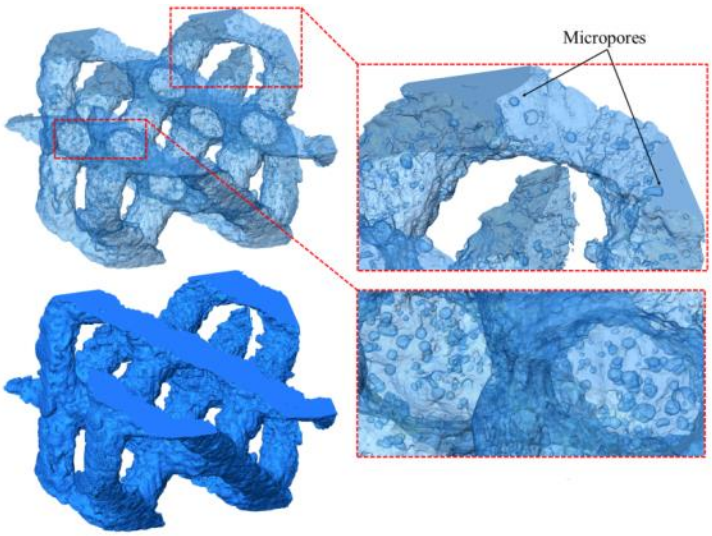

Fig. 11. Micropores in geometric models obtained on the basis of microtomographic images on the example of a diamond structure with a relative density of 27%.

Based on the generated geometric models, the values of the relative density of diamond structures obtained on the basis of CT and micro-CT images were determined and compared with the nominal values obtained for the produced materials (Table 3). Relative density was measured experimentally as the ratio of the measured specimen mass and the nominal volume value without taking into account the voids of the structure (as if it were a solid material) and then related to the density of the solid material. For models derived from micro-CT and CT, relative density was measured in Avizo software based on binary image analysis. For this purpose, the total volume of voxels representing the solid material in the lattice structure was compared to the volume of voxels identified as voids in the material. Attention should be paid to overestimating the relative density obtained for all analyzed methods in comparison to the assumed (nominal) value. This is due to the struts oversizing resulting from the production process depending mainly on the struts orientation and additive manufacturing parameters [46]. The results shown in Table 3 indicate an increase in the difference between the nominal and experimental relative density values with the increase in relative density. It can also be noticed that the greater accuracy of the micro-CT device in relation to CT, allowed to obtain results very similar to the experimental values. Whereas, the discrepancy in the relative density values determined on the basis of CT images and experimentally, results from the limited accuracy of the tomographic measurement and the lack of taking into account the micropores in the model's volume generated by this method.

Table 3. Comparison of the relative density values of geometric models and produced material specimens.

Relative density ρ_{rel} [%]			
Nominal	Experimental	based on CT	based on micro-CT
18.5	20.81	21.68	21.62
27	30.54	31.28	30.93
50	54.26	59.80	54.95
66	72.95	77.53	71.95

3.3. Numerical modeling of the tensile deformation process of diamond lattice structures

In numerical modeling, a workstation equipped with Intel Core i9-7940X CPU, SSD M.2 drive, and 64GB DDR4 memory was used. The previously generated geometric models were imported to the software using FEM (MSC.MARC) in the form of surface finite element meshes. Then, based on the surface meshes, solid finite element meshes were generated. Four-node tetrahedral solid finite elements of the Tetra 134 type [54] were used for numerical calculations. The average size of the finite elements for structures generated from CT images was approximately 0.1 mm and 0.02 mm for

models based on micro-CT images. Representative elements of the lattice structures obtained from CT images were divided into approximately 0.94, 1.15, 1.48, and 1.54 million finite elements for the relative material density of 18.5%, 27%, 50%, and 66%, respectively. However, in the case of structures obtained on the basis of computed microtomography, it was 6.13, 6.4, 8.72, and 9.04 million finite elements respectively. In Fig. 12 shown comparison of exemplary diamond structures divided into finite elements.

In order to determine the influence of the finite element size on the results of numerical calculations, additional calculations were carried out for meshes with larger and smaller finite elements than those described above. For this, elements of 0.01 mm and 0.05 mm (micro-CT models) as well as 0.05 and 0.25 mm (CT models) were used. It should be noted that reducing the size of finite elements by half compared to those used in the manuscript resulted in a change in the Young's modulus, yield stress and maximum effective stress by less than 1% (based on mean absolute percentage error). On the other hand, increasing the size of the finite element significantly influenced the overestimation of the research results. In the case of models based on micro-CT, it was an average increase of 4.55%, while in the case of CT the average error was 12.79%.

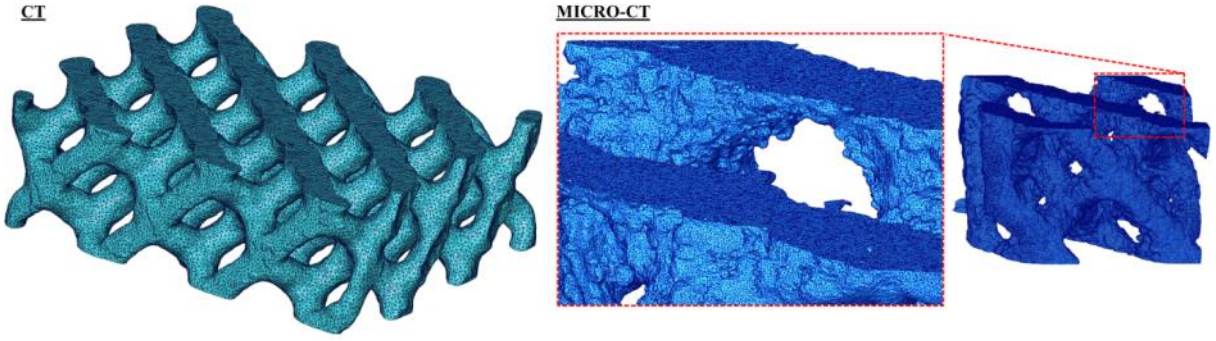

Fig. 12. Division into finite elements of geometric models of lattice structures with a relative density of 27% obtained with the use of both tomographic techniques.

In the work, the tensile deformation process of Ti-6Al-4V diamond structures obtained by 3D printing was modeled. For this purpose, two variants of boundary conditions were used (Fig. 13). The first variant was determined for models generated on the basis of CT images, and the second based on micro-CT images. In the first variant, a symmetric boundary condition (SBC) was used on one of the model base plane, which prevents the model displacement in the direction of the z-axis. Nodal displacements in the direction of positive z-axis values were applied to the finite element nodes lying on the second model base plane, thus causing the macroscopic tension of the model. In order to prevent the rotation of the model during deformation, nodes lying on two planes crossing the center of the model (Fig. 13) were applied displacements equal to zero in the x- and y-directions. Due to the four times smaller cross-section of the geometric models obtained with the use of micro-CT images (than in the case of models based on CT images), symmetrical boundary conditions were applied.

They were defined on the three faces of the model by applying displacements equal to zero for the nodes lying on them, in directions normal to these planes (Fig. 13). The tension of the model, as in the previous case, was obtained by applying nodal displacements in the z-direction to the nodes lying on the upper base plane of the geometric model.

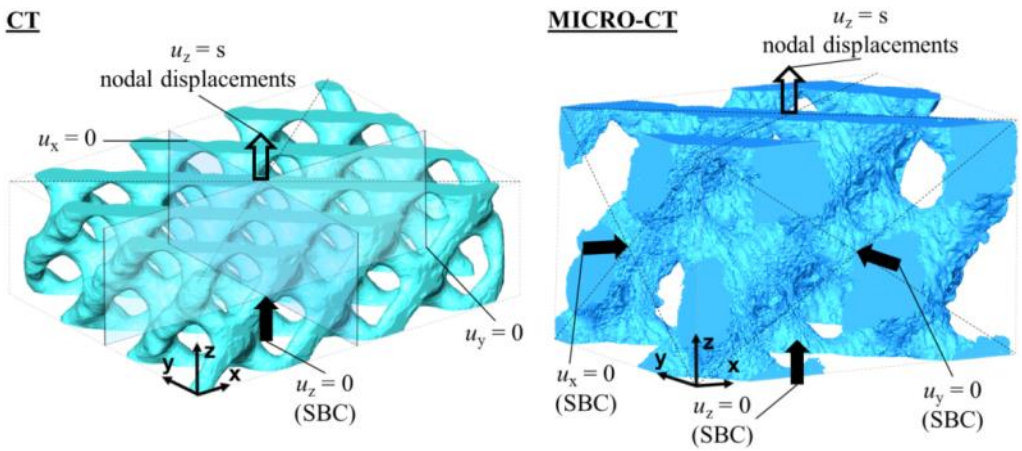

Fig. 13. Boundary conditions used for tensile modeling of lattice structures obtained by computed tomography (on the left) and microtomography (on the right) .

In numerical modeling of the tensile behavior of lattice structures obtained from CT and micro-CT images, an elastic-plastic model of the material with isotropic hardening was used. Young's modulus E_s = 116.9 GPa and Poisson's ratio ν_s = 0.31 obtained as a result of experimental tests of solid Ti-6Al-4V specimens (relative density near to 0) obtained by 3D printing were used for the calculations. The Huber-von Mises plasticity criterion was also used, and the material nonlinearity was defined using the true stress-strain curve (Fig. 8).

4. NUMERICAL RESULTS

This chapter describes the obtained results of numerical calculations concerning the tensile deformation process of Ti-6Al-4V diamond structures with various relative densities. The stress and strain distributions in deformed materials as well as the material tensile curves were shown and analyzed. Stress concentration and potential fracture initiation locations were also indicated.

4.1. Stress and strain distributions in deformed lattice structures

Fig. 14 shows the equivalent Huber-von Mises stress distributions in cellular structures at the moment of obtaining an effective strain of 0.01. The places with the highest stress value are near the nodes of the diamond structures. In the case of structures based on CT scanning, these are the notches in the shape of node surfaces, while in the structures based on micro-CT, imperfections on the surface create scattered micronotches concentrating the stress. It can also be seen that with the increase in the relative density of the material, the value of the equivalent stress in the places of concentration

increases. The increase in the stress value according to the Huber-von Mises hypothesis with the increase in relative density is related to the topology of the obtained diamond structure. Changing the shape of the structure by changing the thickness of the struts results in a higher stress concentration associated with the change in the notch geometry of the structure. The distributions of the equivalent plastic strain at the moment of obtaining an effective strain of 0.01 (Figs. 15 and 16) are of a similar character to the distributions of equivalent stress. The strain fields show that with the increase of the relative density of the material, the areas of plastic zones in the material become larger.

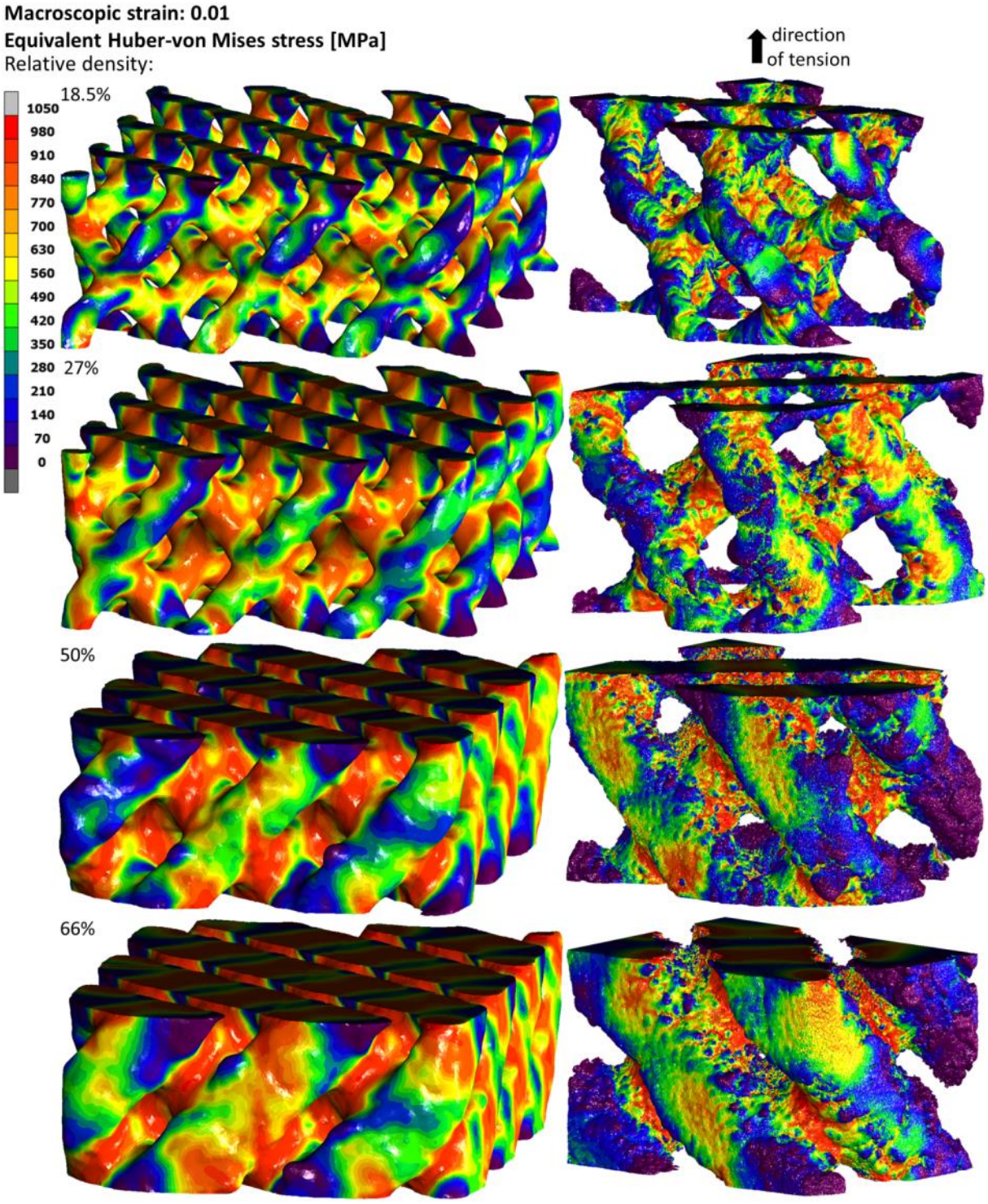

Fig. 14. Equivalent stress distributions according to the Huber-von Mises hypothesis in lattice structures obtained on the basis of computed tomography (on the left) and microtomography (on the right) at the moment of obtaining an effective strain of 0.01.

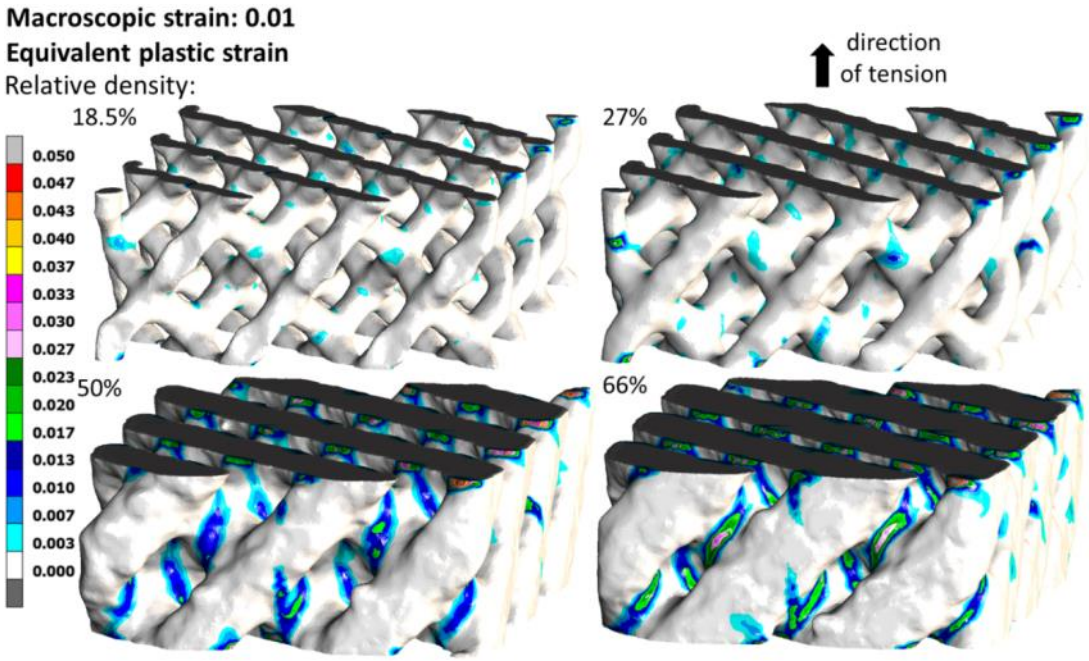

Fig. 15. Equivalent plastic strain distributions in lattice structures obtained on the basis of tomography at the moment of obtaining an effective strain of 0.01.

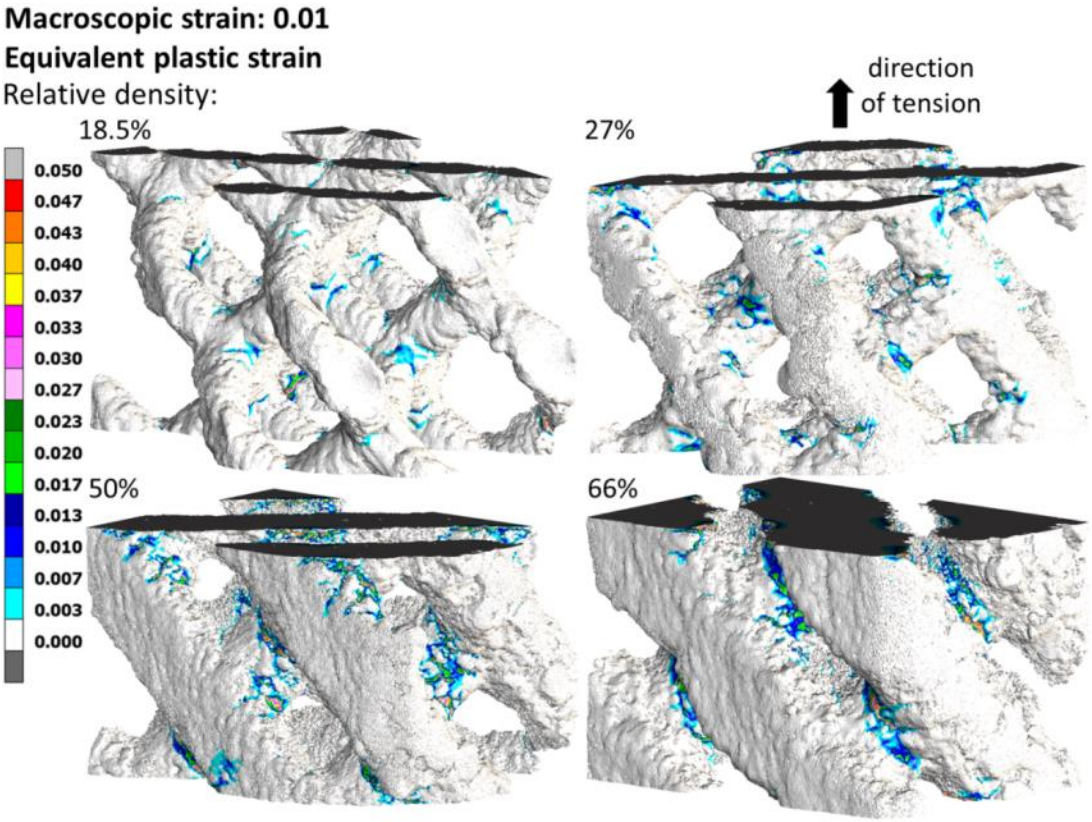

Fig. 16. Equivalent plastic strain distributions in lattice structures obtained on the basis of microtomography at the moment of obtaining an effective strain of 0.01.

In Fig. 17 shown the equivalent stress distributions in the tensile diamond structures at the moment of obtaining the maximum effective strain determined experimentally. The places where the material hardening is the greatest and the equivalent stress reaches its highest values are near the structure nodes (Fig. 17). Higher stress values occur in structures mapped on the basis of micro-CT. This is due to the greater concentration of stress at the locations in the shape of micronotches that result from the manufacturing process. With the relative density of the material increases, the values of the equivalent stress increase. This is mainly due to the notch (in the macroscale) effect which occurs between struts and nodes of the lattice structures. As the struts thickness increases, their length decreases, which results in the formation of notches with smaller radii and a higher stress concentration.

Distributions of the maximum principal stress in lattice structures obtained on the basis of the two tested methods are shown in Fig. 18. As in the case of the previously analyzed stress, the maximum values are located near the nodes of the examined structures. However, it should be noted that the obtained maximum values exceed the critical value of the maximum principal stress σ_{1c} = 1612 MPa obtained for solid Ti-6Al-4V specimens manufactured by the LPBF. In locations where the maximum principal stress exceeds the critical value (red arrows), fracture may be initiated. A large number of such locations have been observed in models based on micro-CT, focusing mainly on the surface of struts around structure nodes. In materials with a relative density of 18.5% and 27%, the critical stress sometimes occurs at greater distances from the nodes of diamond structures. It is related to the significant influence of technological micronotches on the stress distribution in the material and its strength. Whereas, in materials with higher relative density, i.e., 50% and 66%, macroscopic notches have a decisive influence on the strength of the structures. The indicated locations and their distribution show a significant similarity to the results of the experimental studies described in the previous chapter (Fig. 4). In contrast, in the case of models obtained from CT images, there are fewer locations where the critical stress value is exceeded. In structures where ρ_{rel} is 18.5% and 27%, there are only a few such places and for materials with ρ_{rel} = 50% and 66% they are more concentrated and occupy a larger area than in the corresponding models based on micro-CT.

The maps of the maximum shear stress (Fig. 19) show that the locations of the maximum values partially coincide with the locations of the maximum principal stress σ_{1c}.

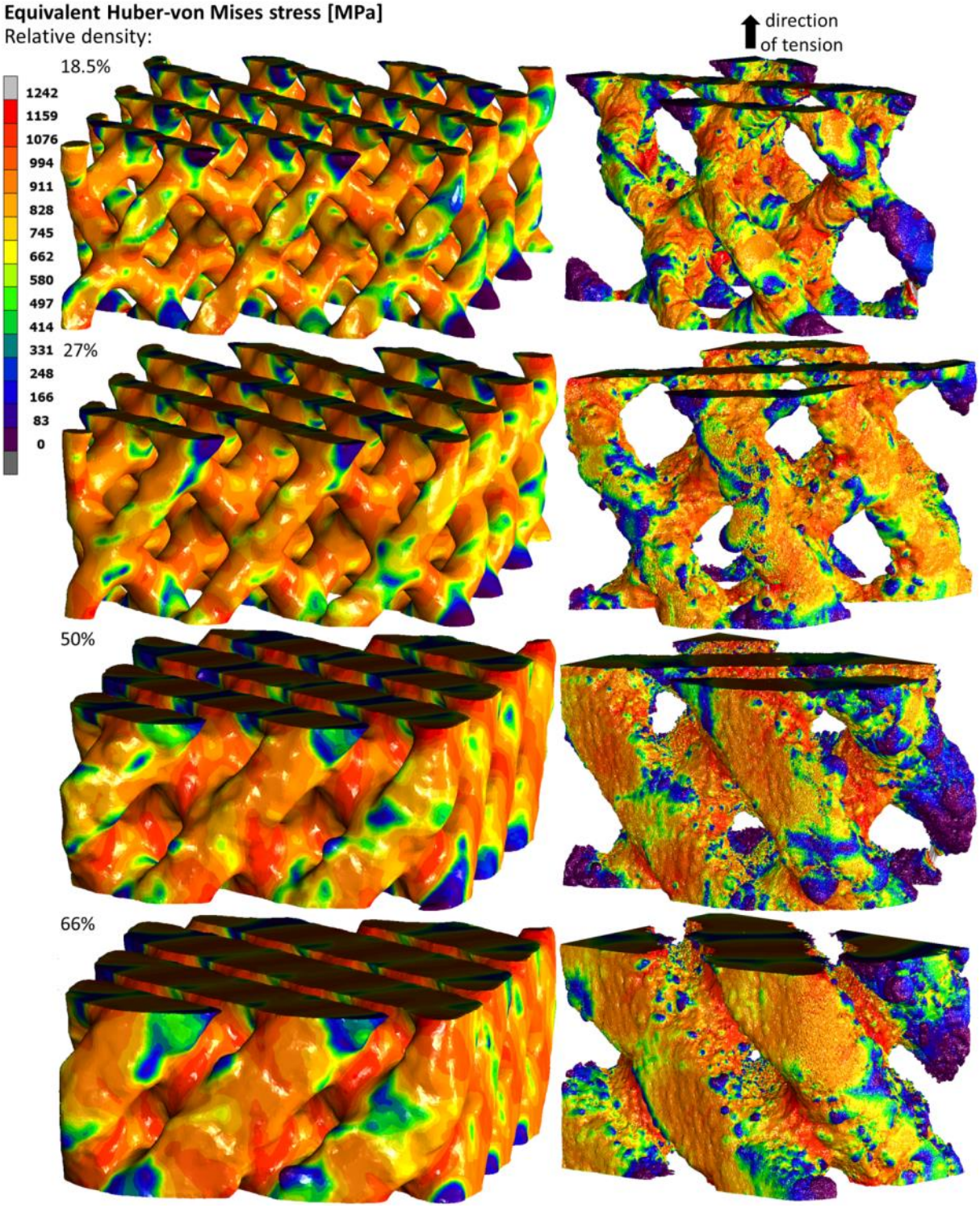

Fig. 17. Equivalent stress distributions according to the Huber-von Mises hypothesis in lattice structures obtained on the basis of computed tomography (on the left) and microtomography (on the right) at the moment of macroscopic fracture initiation.

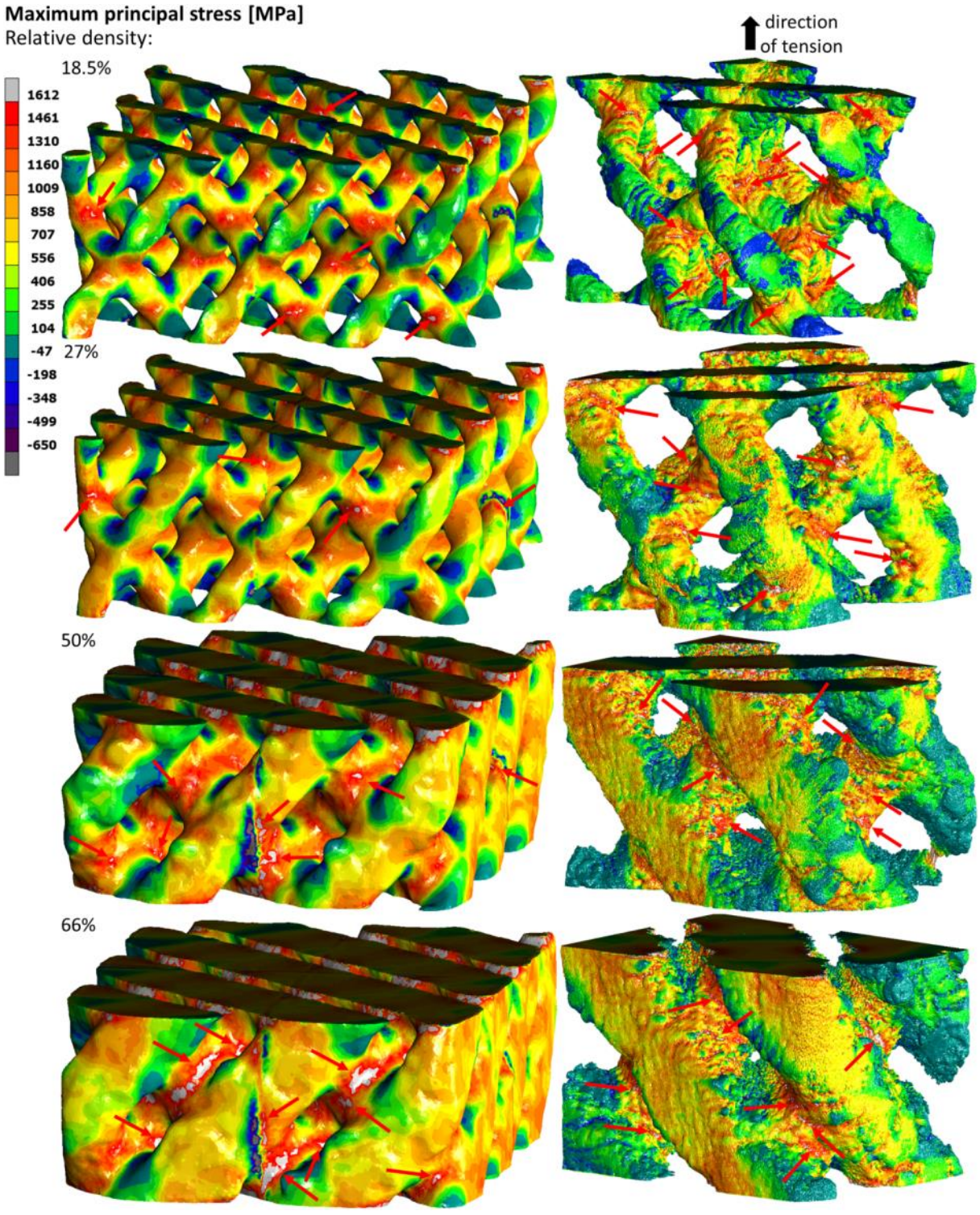

Fig. 18. Maximum principal stress distributions in lattice structures obtained on the basis of computed tomography (on the left) and microtomography (on the right) at the moment of macroscopic fracture initiation.

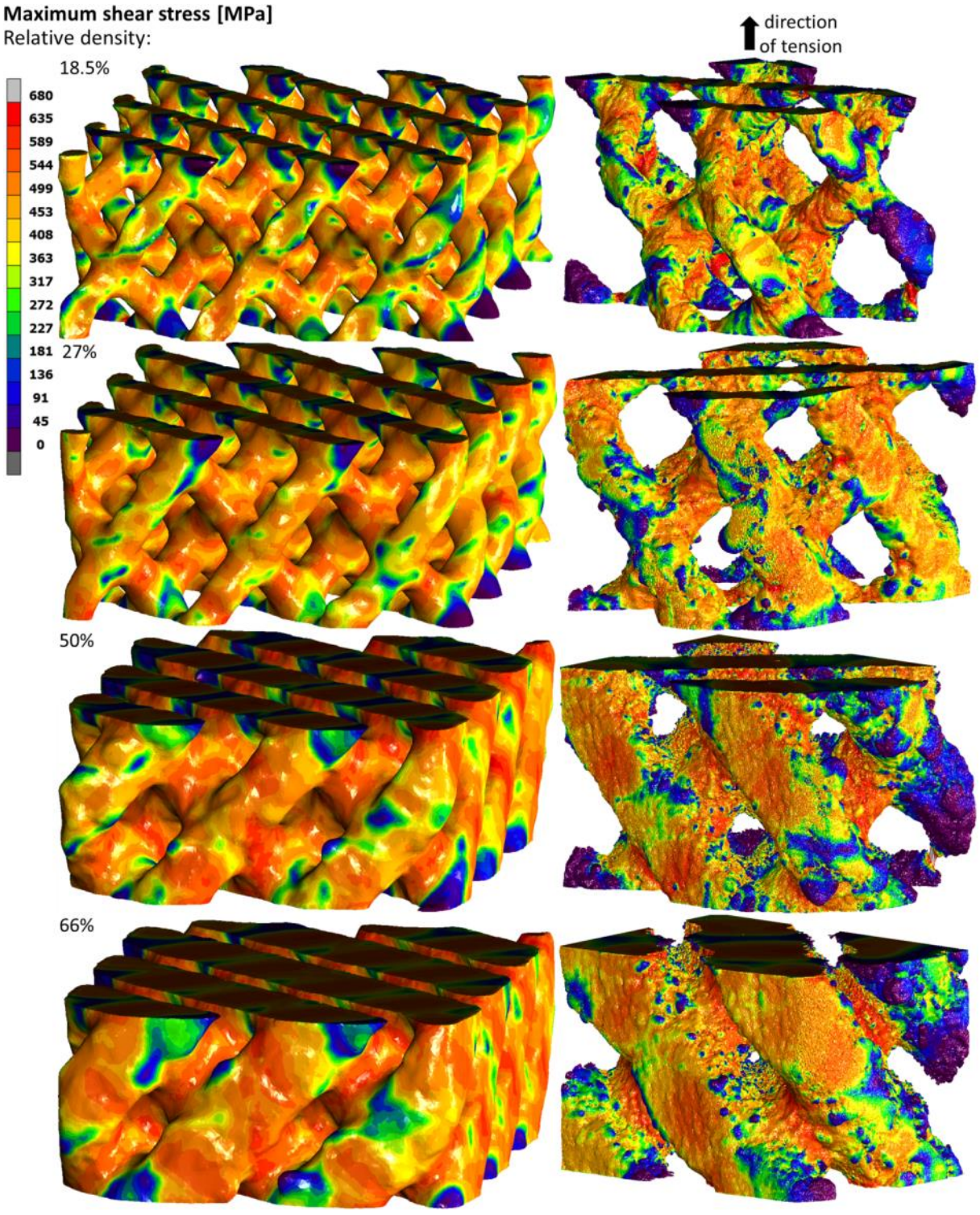

Fig. 19. Maximum shear stress distributions in lattice structures obtained on the basis of computed tomography (on the left) and microtomography (on the right) at the moment of macroscopic fracture initiation.

In Figs. 20 and 21 shown the plastic strain distributions for structures based on CT and micro-CT images, respectively at the moment of macroscopic fracture initiation. In the case of CT models, with an increase in relative density, the plastic zones and the maximum values of strain significantly increase. For the micro-CT models, the zones increase less with increasing relative density, and the strain values achieve similar values. It should be noted that the deformation values in the most plastically deformed places are even twice as high in the case of models based on micro-CT images than in the case of CT images. This is due to the high concentration of plastic deformation in the micronotches of the investigated structures, which in the case of CT models are smoothed due to the lower accuracy of the tomographic measurement.

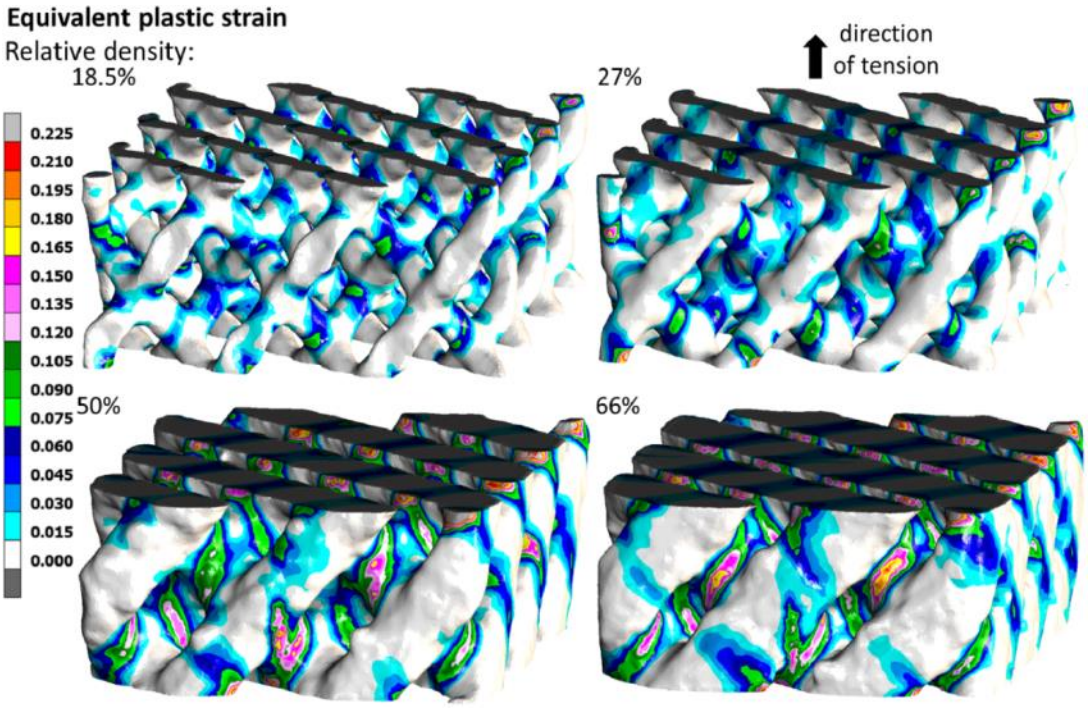

Fig. 20. Equivalent plastic strain distributions in lattice structures obtained on the basis of tomography at the moment of macroscopic fracture initiation.

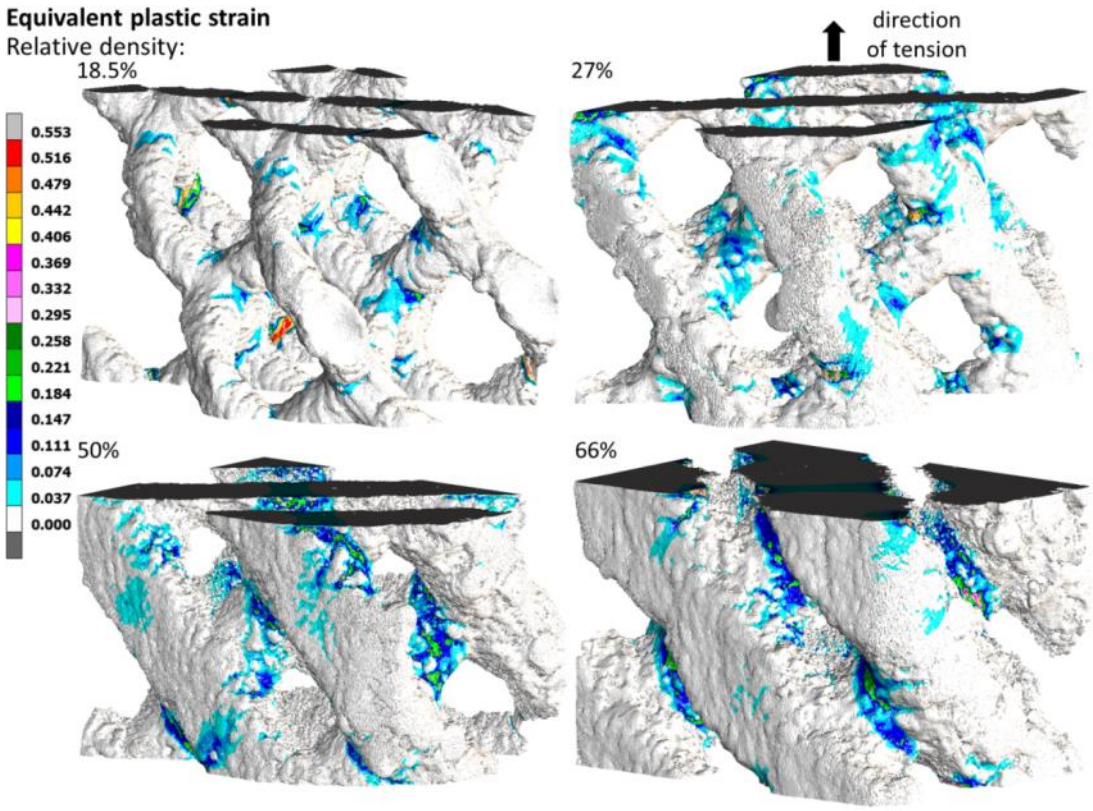

Fig. 21. Equivalent plastic strain distributions in lattice structures obtained on the basis of microtomography at the moment of macroscopic fracture initiation.

4.2. Effective stress-strain curves of tensile lattice structures

In Fig. 22 shown charts of the relationship between effective stress and effective strain obtained by numerical calculations and experimental tests. It should be emphasized that in the case of models based on micro-CT, a satisfactory agreement of the computational and experimental results was obtained. In the case of models based on CT images, there is a significant discrepancy between the modeling and experimental results. The curves shown are also an experimental verification of the applied calculation models. It can be seen that the smoothing of the structures shape and the overestimation of the relative density caused by the lower accuracy of the measurement with the CT device causes the calculated values of the effective stress to be overestimated. The high compliance of the stress-strain curves obtained on the basis of computational models using microtomographic images means that taking into account structure microdefects in the calculations has a significant impact on the deformation process of diamond lattice structures. To correctly simulate the deformation process of this type of material, the imperfections resulting from the material production process should be taken into account.

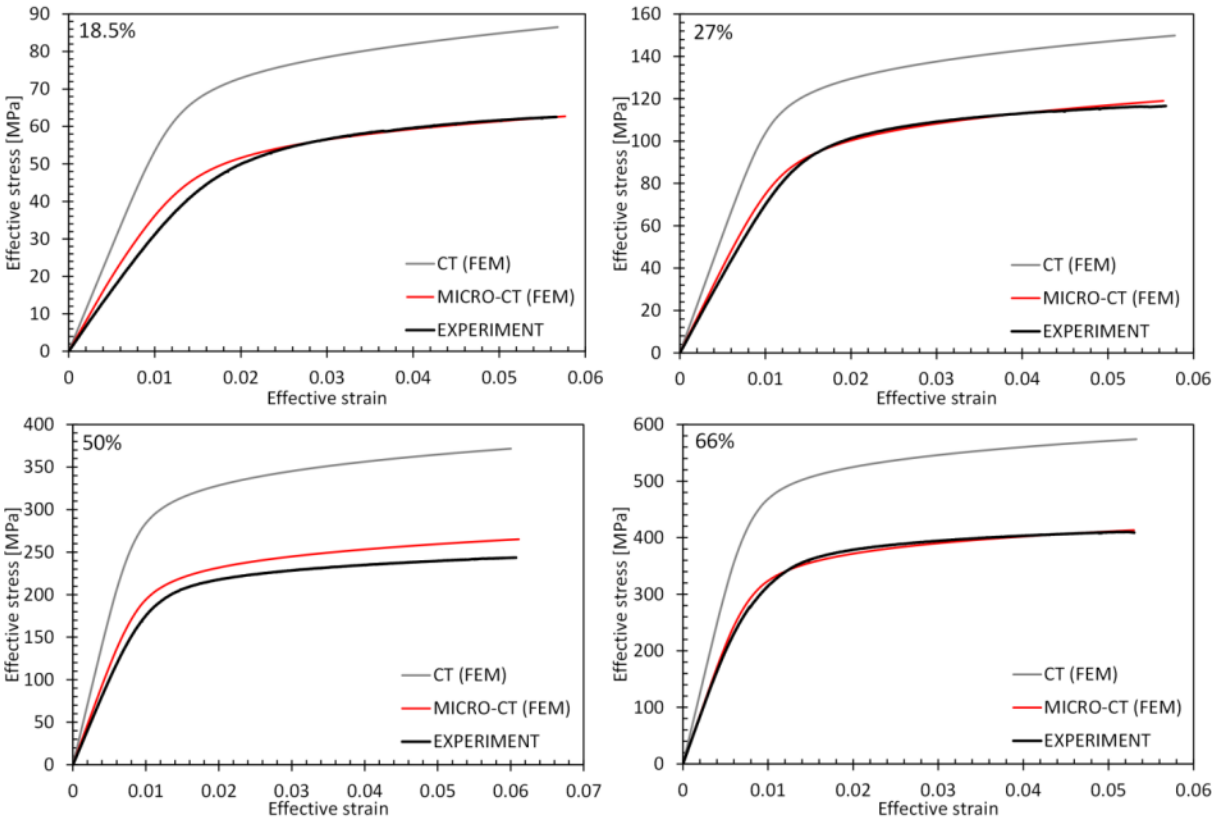

Fig. 22. Comparison of nominal effective stress-strain curves of the investigated diamond structures obtained by numerical calculations and experimental tests.

4.3. Effective mechanical properties

Based on the performed numerical calculations, the effective mechanical properties of diamond structures such as Young's modulus, yield stress and ultimate tensile strength were also determined (Table 4). It can be noticed that the inclusion of details of the lattice structures geometry by means of the micro-CT device in numerical calculations significantly improves the convergence of the results with experimental tests compared to the calculations using CT images. Based on the calculated percentage errors shown in Table 5, the mean absolute percentage error (MAPE) was also determined for the strength properties obtained with the use of two tomographic methods. The MAPE obtained for the models based on the CT images in the case of Young's modulus is $E_{\mathrm{MAPE}}^{\mathrm{CT}} = 54.0\%$, yield stress $\sigma_{0.2\mathrm{MAPE}}^{\mathrm{CT}} = 46.0\%$ and ultimate tensile strength $\sigma_{\mathrm{maxMAPE}}^{\mathrm{CT}} = 39.6\%$. Whereas, for the models obtained on the basis of computed microtomography, it was respectively $E_{\mathrm{MAPE}}^{\text{micro-CT}} = 7.5\%$, $\sigma_{0.2\mathrm{MAPE}}^{\text{micro-CT}} = 3.1\%$, $\sigma_{\mathrm{maxMAPE}}^{\text{micro-CT}} = 2.8\%$. It follows that the lower accuracy of the CT device causes, among others, the smoothing of the surface's shape of the structures and the lack of taking into account the micropores, which significantly increases the value of the obtained effective mechanical

properties. In addition, the micronotches resulting from the material manufacturing process and other structural defects have a significant impact on their mechanical properties.

Table 4. Effective mechanical properties of the studied diamond structures obtained by numerical calculations and experimental tests.

Relative density ρ_{rel} [%]	Young's modulus E_{eff} [GPa]			Yield stress $\sigma_{0.2eff}$ [MPa]			Maximum effective stress σ_{eff}^{max} [MPa]		
	Exp.	CT	micro-CT	Exp.	CT	micro-CT	Exp.	CT	micro-CT
18.5	3.7	5.55	4.0	42.4	65.2	43.3	62.5	86.5	62.7
27	7.4	11.12	8.1	89.2	115.3	87.2	117.2	149.9	119.0
50	20.4	34.8	23.1	193.5	285.7	197.8	244.2	371.7	265.0
66	41.8	60.8	41.9	300.8	460.8	318.1	410.0	574.1	413.3

Table 5. Percentage error obtained for the effective mechanical properties of the investigated lattice structures.

Percentage error [%]						
Relative density ρ_{rel} [%]	Young's modulus E_{eff}		Yield stress $\sigma_{0.2eff}$		Max effective stress σ_{eff}^{max}	
	CT	micro-CT	CT	micro-CT	CT	micro-CT
18.5	50.0	7.3	53.8	2.1	38.4	0.3
27	50.3	9.1	29.3	2.2	27.9	1.5
50	70.3	13.4	47.6	2.2	52.2	8.5
66	45.5	0.3	53.2	5.8	40.0	0.8

The values of the effective Young's modulus and the ultimate tensile strength obtained as a result of numerical calculations were also compared with the curve approximating the experimental values [15]. To better show the dependence of the mechanical properties on the relative material density, the charts (Fig. 23) show the values of Young's modulus and ultimate tensile strength related to the corresponding values obtained for the solid Ti-6Al-4V alloy. The form of these relations is as follows: for Young's modulus $E_{eff}^{ratio} = E_{eff} / E_s$ and for ultimate tensile strength $\sigma_{max}^{ratio} = \sigma_{eff}^{max} / \sigma_s^{max}$, where E_s and σ_s^{max} are respectively Young's modulus and nominal ultimate tensile strength obtained for solid Ti-6Al-4V specimens. The approximation curves in both cases were obtained as power functions, which were determined on the basis of nonlinear least squares curve fitting. The approximating functions for the effective Young's modulus have the form $E_{approx}^{ratio} = \rho_{rel}^{2.856}$ and for ultimate tensile strength $\sigma_{approx}^{ratio} = \rho_{rel}^{2.265}$.

From the charts (Fig. 23), it can be concluded that the character of changes in the obtained results of numerical calculations is similar to the shape of the approximation curve based on experimental studies. The greatest discrepancies in relation to the curve occur for the models obtained on the basis of CT images. It should also be noted that for these models the convergence of the

obtained values with the approximation increases with the increase of the relative density. This indicates that the impact of the lack of detail mapping of the structure shape on the values of the mechanical properties of cellular materials in these models decreases. Whereas, for the models obtained on the basis of micro-CT images, the values of the obtained relationships $E_{\mathrm{eff}}^{\mathrm{ratio}}$ and $\sigma_{\mathrm{max}}^{\mathrm{ratio}}$ are very similar to the values obtained as a result of experimental tests, which means that the trend is also very similar. The results obtained on the basis of the micro-CT models also indicate the correct simulation of the deformation process of tensile diamond structures using these calculation models.

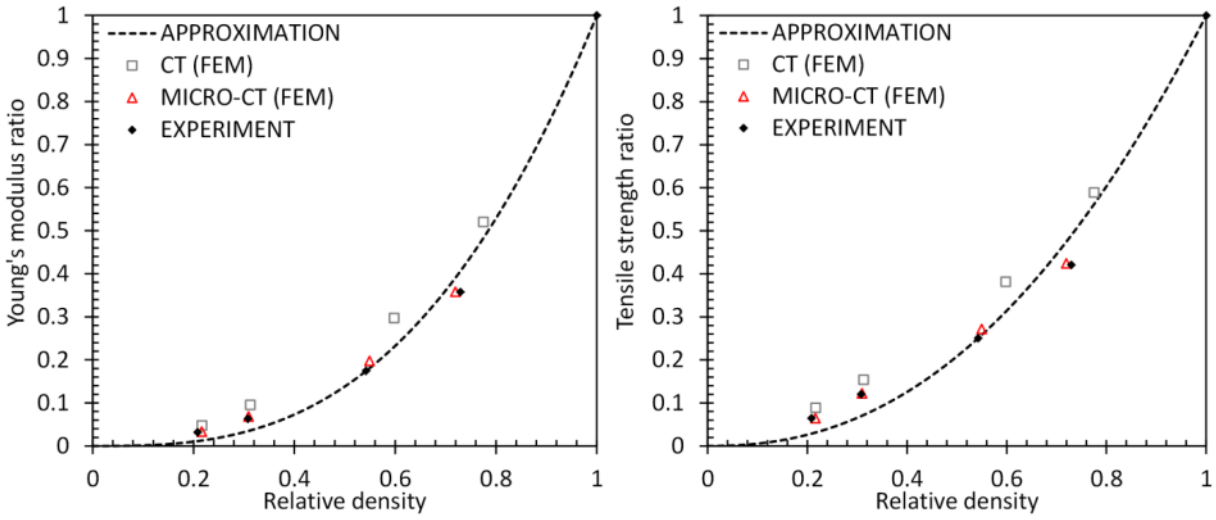

Fig. 23. Summary of the dependence of effective Young's modulus ratio (on the left) and ultimate tensile strength ratio (on the right) on the relative density of the tested materials obtained numerically and experimentally.

5. CONCLUSIONS

This work presents the results of numerical modeling using the finite element method of the deformation process of diamond structures of the Ti-6Al-4V titanium alloy with various relative densities (porosity: 0%, 34%, 50%, 73%, 81.5%) obtained by the additive method laser power bed fusion (LPBF). In numerical calculations, geometric models recreating the realistic shape of the investigated structures were used. These models were obtained on the basis of images obtained by means of computed tomography (CT) and microtomography (micro-CT), i.e., on two levels of accuracy of mapping the shape details of the investigated structures.

Based on the research carried out and described in the work and the analysis of the obtained results, the following conclusions can be presented:

1. It has been shown that the accuracy of the geometry mapping by computed tomography is insufficient, as evidenced by the significantly overestimated values of the relative density and tensile force in the charts of the relationship between nominal effective stress and strain.

Moreover, the strength properties of the structure determined on this basis significantly differ from those determined experimentally.

2. Modeling of stress and strain fields using the finite element method and geometric models mapping the real shape of the studied structures obtained by computed microtomography (micro-CT) enables the determination of effective mechanical properties of structures of any geometry, such as: effective axial modulus of elasticity, effective ultimate tensile strength, effective yield strength and effective relative elongation, based on the known values of these parameters for a solid material. This has practical applications, e.g., when metallic materials are used as replacements for joint endoprosthesis. Lattice structures make it possible to decrease the stiffness of the material to the level of bone tissue stiffness, which would ensure better cooperation of the implant-bone connections (lower bone load). At the same time, however, there is a decrease in the strength properties of the structure, hence it is so important to choose its geometry optimally so that it is able to withstand the applied load.
3. In the case of using in the calculations the mapping of the structure geometry by means of computed microtomography, the obtained maximum values of local stress (maximum principal and equivalent) were similar to the values of these stress for the solid material at the moment of fracture initiation. This means that it is possible to predict the true strength of the obtained structure on the basis of numerical calculations, without conducting experimental tests.
4. The obtained results of the stress concentration and deformations in the realistic structure also allow the analysis of the fatigue properties of the material, taking into account both the notches related to the shape of the diamond structure itself, as well as voids and technological micronotches between the particles of the molten powder, resulting from the inaccuracy of mapping the surfaces of the struts using laser power bed fusion (LPBF) method. The stress and strain concentrations caused by them significantly reduce the fatigue life of the structure, especially in the field of high-cycle fatigue. However, to determine the quantitative dependence of the number of load cycles causing the fracture initiation on the amplitude of this load, experimental tests in this area are necessary.
5. The obtained results can be the basis for modifying the structure geometry in terms of reducing the effect of structural notches - stress and strain concentration, and at the same time increasing its strength and fatigue life. This requires, of course, additional calculations by the finite element method to confirm the reduction of stress and strain concentration, as well as experimental fatigue tests of the corrected structure confirming the increase in fatigue life. However, a much more difficult problem is the limitation of the influence of technological micronotches, resulting directly from the specificity of the LPBF method. The titanium powder particles are of finite size and obtaining a smoother surface would require additional processing, difficult to perform in the production of a diamond-like metamaterial or the use of a powder with smaller particles, which would significantly increase the manufacturing cost.

REFERENCES

[1] X. Wang, S. Xu, S. Zhou, W. Xu, M. Leary, P. Choong, M. Qian, M. Brandt, Y.M. Xie, Topological design and additive manufacturing of porous metals for bone scaffolds and orthopaedic implants: A review, Biomaterials. (2016). doi:10.1016/j.biomaterials.2016.01.012.

[2] F. Li, J. Li, T. Huang, H. Kou, L. Zhou, Compression fatigue behavior and failure mechanism of porous titanium for biomedical applications, J. Mech. Behav. Biomed. Mater. (2017). doi:10.1016/j.jmbbm.2016.09.035.

[3] H. Shahali, A. Jaggessar, P.K.D.V. Yarlagadda, Recent Advances in Manufacturing and Surface Modification of Titanium Orthopaedic Applications, in: Procedia Eng., 2017. doi:10.1016/j.proeng.2017.01.259.

[4] R.M. Diaz-Sanchez, A. De-Paz-carrion, M.A. Serrera-Figallo, D. Torres-Lagares, A. Barranco, J.R. León-Ramos, J.L. Gutierrez-Perez, In vitro and in vivo study of titanium grade IV and titanium grade v implants with different surface treatments, Metals (Basel). (2020). doi:10.3390/met10040449.

[5] W.S.W. Harun, M.S.I.N. Kamariah, N. Muhamad, S.A.C. Ghani, F. Ahmad, Z. Mohamed, A review of powder additive manufacturing processes for metallic biomaterials, Powder Technol. (2018). doi:10.1016/j.powtec.2017.12.058.

[6] F. Bartolomeu, C.S. Abreu, C.G. Moura, M.M. Costa, N. Alves, F.S. Silva, G. Miranda, Ti6Al4V-PEEK multi-material structures – design, fabrication and tribological characterization focused on orthopedic implants, Tribol. Int. (2019). doi:10.1016/j.triboint.2018.11.017.

[7] ISO/ASTM 52911-1:2019, Additive manufacturing – Design – Part 1: Laser-based powder bed fusion of metals., (n.d.).

[8] H. Attar, M. Calin, L.C. Zhang, S. Scudino, J. Eckert, Manufacture by selective laser melting and mechanical behavior of commercially pure titanium, Mater. Sci. Eng. A. (2014). doi:10.1016/j.msea.2013.11.038.

[9] M. Fousová, D. Vojtěch, J. Kubásek, E. Jablonská, J. Fojt, Promising characteristics of gradient porosity Ti-6Al-4V alloy prepared by SLM process, J. Mech. Behav. Biomed. Mater. (2017). doi:10.1016/j.jmbbm.2017.01.043.

[10] S. Singh, S. Ramakrishna, Biomedical applications of additive manufacturing: Present and future, Curr. Opin. Biomed. Eng. (2017). doi:10.1016/j.cobme.2017.05.006.

[11] A. Falkowska, A. Seweryn, Fatigue of sintered porous materials based on 316l stainless steel under Uniaxial loading, Mater. Sci. (2015). doi:10.1007/s11003-015-9829-5.

[12] X. Yan, Q. Li, S. Yin, Z. Chen, R. Jenkins, C. Chen, J. Wang, W. Ma, R. Bolot, R. Lupoi, Z. Ren, H. Liao, M. Liu, Mechanical and in vitro study of an isotropic Ti6Al4V lattice structure fabricated using selective laser melting, J. Alloys Compd. (2019). doi:10.1016/j.jallcom.2018.12.220.

[13] A. Falkowska, A. Seweryn, A. Tomczyk, Fatigue life and strength of 316L sintered steel of varying porosity, Int. J. Fatigue. (2018). doi:10.1016/j.ijfatigue.2018.02.023.

[14] Z.J. Wally, A.M. Haque, A. Feteira, F. Claeyssens, R. Goodall, G.C. Reilly, Selective laser melting processed Ti6Al4V lattices with graded porosities for dental applications, J. Mech. Behav. Biomed. Mater. (2019). doi:10.1016/j.jmbbm.2018.08.047.

[15] A. Falkowska, A. Seweryn, M. Skrodzki, Strength Properties of a Porous Titanium Alloy Ti6Al4V with Diamond Structure Obtained by Laser Power Bed Fusion (LPBF), Materials (Basel). 13 (2020) 5138. doi:https://doi.org/10.3390/ma13225138.

[16] L. Bai, J. Zhang, X. Chen, C. Yi, R. Chen, Z. Zhang, Configuration optimization design of Ti6Al4V lattice structure formed by SLM, Materials (Basel). (2018). doi:10.3390/ma11101856.

[17] X. Cao, S. Duan, J. Liang, W. Wen, D. Fang, Mechanical properties of an improved 3D-printed rhombic dodecahedron stainless steel lattice structure of variable cross section, Int. J. Mech. Sci. (2018). doi:10.1016/j.ijmecsci.2018.07.006.

[18] S.Y. Chen, J.C. Huang, C.T. Pan, C.H. Lin, T.L. Yang, Y.S. Huang, C.H. Ou, L.Y. Chen, D.Y. Lin, H.K. Lin, T.H. Li, J.S.C. Jang, C.C. Yang, Microstructure and mechanical properties of open-cell porous Ti-6Al-4V fabricated by selective laser melting, J. Alloys Compd. (2017). doi:10.1016/j.jallcom.2017.04.190.

[19] R. Hedayati, S.M. Ahmadi, K. Lietaert, B. Pouran, Y. Li, H. Weinans, C.D. Rans, A.A. Zadpoor, Isolated and modulated effects of topology and material type on the mechanical properties of additively manufactured porous biomaterials, J. Mech. Behav. Biomed. Mater. (2018). doi:10.1016/j.jmbbm.2017.12.029.

[20] Q. Ran, W. Yang, Y. Hu, X. Shen, Y. Yu, Y. Xiang, K. Cai, Osteogenesis of 3D printed porous Ti6Al4V implants with different pore sizes, J. Mech. Behav. Biomed. Mater. (2018). doi:10.1016/j.jmbbm.2018.04.010.

[21] B. Zhang, X. Pei, C. Zhou, Y. Fan, Q. Jiang, A. Ronca, U. D'Amora, Y. Chen, H. Li, Y. Sun, X. Zhang, The biomimetic design and 3D printing of customized mechanical properties porous Ti6Al4V scaffold for load-bearing bone reconstruction, Mater. Des. (2018). doi:10.1016/j.matdes.2018.04.065.

[22] B. Van Hooreweder, Y. Apers, K. Lietaert, J.P. Kruth, Improving the fatigue performance of porous metallic biomaterials produced by Selective Laser Melting, Acta Biomater. (2017). doi:10.1016/j.actbio.2016.10.005.

[23] E. Askari, I.F. Cengiz, J.L. Alves, B. Henriques, P. Flores, M.C. Fredel, R.L. Reis, J.M. Oliveira, F.S. Silva, J. Mesquita-Guimarães, Micro-CT based finite element modelling and experimental characterization of the compressive mechanical properties of 3-D zirconia scaffolds for bone tissue engineering, J. Mech. Behav. Biomed. Mater. (2020). doi:10.1016/j.jmbbm.2019.103516.

[24] M. Doroszko, A. Seweryn, Pore-scale numerical modelling of large deformation behaviour of sintered porous metals under compression using computed microtomography, Mech. Mater. (2020). doi:10.1016/j.mechmat.2019.103259.

[25] A. Legwand, K. Perzyński, Ł. Madej, Development of communication mechanism for the fully coupled multiscale model of 3D compression test, SN Appl. Sci. (2020). doi:10.1007/s42452-020-3178-1.

[26] M. Zhou, H. Zhou, Experimental investigation and numerical modeling of strength properties of iron ore sinter based on pilot-scale pot tests and X-ray computed tomography, J. Mater. Res. Technol. (2020). doi:10.1016/j.jmrt.2020.09.054.

[27] M. Zhou, H. Zhou, Flame front propagation and sinter strength properties of permeable sintering bed prepared via enhanced granulation with hydrated lime, Asia-Pacific J. Chem. Eng. (2020). doi:10.1002/apj.2592.

[28] P. Baranowski, P. Płatek, A. Antolak-Dudka, M. Sarzyński, M. Kucewicz, T. Durejko, J. Małachowski, J. Janiszewski, T. Czujko, Deformation of honeycomb cellular structures manufactured with Laser Engineered Net Shaping (LENS) technology under quasi-static loading: Experimental testing and simulation, Addit. Manuf. (2019). doi:10.1016/j.addma.2018.11.018.

[29] M. Kucewicz, P. Baranowski, J. Małachowski, A method of failure modeling for 3D printed cellular structures, Mater. Des. (2019). doi:10.1016/j.matdes.2019.107802.

[30] X. Geng, Y. Lu, C. Liu, W. Li, Z. Yue, Fracture characteristic analysis of cellular lattice structures under tensile load, Int. J. Solids Struct. (2019). doi:10.1016/j.ijsolstr.2019.01.006.

[31] S. Drücker, M. Schulze, H. Ipsen, L. Bandegani, H. Hoch, M. Kluge, B. Fiedler, Experimental and numerical mechanical characterization of additively manufactured Ti6Al4V lattice structures considering progressive damage, Int. J. Mech. Sci. (2021). doi:10.1016/j.ijmecsci.2020.105986.

[32] P. Wang, X. Li, S. Luo, M.L.S. Nai, J. Ding, J. Wei, Additively manufactured heterogeneously porous metallic bone with biostructural functions and bone-like mechanical properties, J. Mater. Sci. Technol. (2021). doi:10.1016/j.jmst.2020.05.056.

[33] A. Zankel, J. Wagner, P. Poelt, Serial sectioning methods for 3D investigations in materials science, Micron. 62 (2014) 66–78. doi:10.1016/J.MICRON.2014.03.002.

[34] L. Madej, Digital/virtual microstructures in application to metals engineering – A review, Arch. Civ. Mech. Eng. 17 (2017) 839–854. doi:10.1016/J.ACME.2017.03.002.

[35] Y. Fam, T.L. Sheppard, A. Diaz, T. Scherer, M. Holler, W. Wang, D. Wang, P. Brenner, A. Wittstock, J.D. Grunwaldt, Correlative Multiscale 3D Imaging of a Hierarchical Nanoporous Gold Catalyst by Electron, Ion and X-ray Nanotomography, ChemCatChem. (2018). doi:10.1002/cctc.201800230.

[36] M. Doroszko, A. Seweryn, Modeling of the tension and compression behavior of sintered 316L

using micro computed tomography, Acta Mech. Autom. (2015). doi:10.1515/ama-2015-0012.

[37] M. Doroszko, A. Seweryn, A new numerical modelling method for deformation behaviour of metallic porous materials using X-ray computed microtomography, Mater. Sci. Eng. A. (2017). doi:10.1016/j.msea.2017.02.055.

[38] M. Doroszko, A. Seweryn, Numerical modelling of the mesofracture process of sintered 316L steel under tension using microtomography, Eng. Fract. Mech. (submitted (2020).

[39] Y. Amani, S. Dancette, P. Delroisse, A. Simar, E. Maire, Compression behavior of lattice structures produced by selective laser melting: X-ray tomography based experimental and finite element approaches, Acta Mater. (2018). doi:10.1016/j.actamat.2018.08.030.

[40] L. Boniotti, S. Beretta, L. Patriarca, L. Rigoni, S. Foletti, Experimental and numerical investigation on compressive fatigue strength of lattice structures of AlSi7Mg manufactured by SLM, Int. J. Fatigue. (2019). doi:10.1016/j.ijfatigue.2019.06.041.

[41] K. Hazeli, B.B. Babamiri, J. Indeck, A. Minor, H. Askari, Microstructure-topology relationship effects on the quasi-static and dynamic behavior of additively manufactured lattice structures, Mater. Des. (2019). doi:10.1016/j.matdes.2019.107826.

[42] S. Ruiz de Galarreta, J.R.T. Jeffers, S. Ghouse, A validated finite element analysis procedure for porous structures, Mater. Des. (2020). doi:10.1016/j.matdes.2020.108546.

[43] M. Dallago, B. Winiarski, F. Zanini, S. Carmignato, M. Benedetti, On the effect of geometrical imperfections and defects on the fatigue strength of cellular lattice structures additively manufactured via Selective Laser Melting, Int. J. Fatigue. (2019). doi:10.1016/j.ijfatigue.2019.03.019.

[44] H. Lei, C. Li, J. Meng, H. Zhou, Y. Liu, X. Zhang, P. Wang, D. Fang, Evaluation of compressive properties of SLM-fabricated multi-layer lattice structures by experimental test and μ-CT-based finite element analysis, Mater. Des. (2019). doi:10.1016/j.matdes.2019.107685.

[45] B. Lozanovski, M. Leary, P. Tran, D. Shidid, M. Qian, P. Choong, M. Brandt, Computational modelling of strut defects in SLM manufactured lattice structures, Mater. Des. (2019). doi:10.1016/j.matdes.2019.107671.

[46] L. Xiao, S. Li, W. Song, X. Xu, S. Gao, Process-induced geometric defect sensitivity of Ti–6Al–4V lattice structures with different mesoscopic topologies fabricated by electron beam melting, Mater. Sci. Eng. A. (2020). doi:10.1016/j.msea.2020.139092.

[47] A. Yánez, M.P. Fiorucci, A. Cuadrado, O. Martel, D. Monopoli, Surface roughness effects on the fatigue behaviour of gyroid cellular structures obtained by additive manufacturing, Int. J. Fatigue. (2020). doi:10.1016/j.ijfatigue.2020.105702.

[48] M. Benedetti, V. Fontanari, M. Bandini, F. Zanini, S. Carmignato, Low- and high-cycle fatigue resistance of Ti-6Al-4V ELI additively manufactured via selective laser melting: Mean stress and defect sensitivity, Int. J. Fatigue. (2018). doi:10.1016/j.ijfatigue.2017.10.021.

[49] C. Veyhl, I. V. Belova, G.E. Murch, T. Fiedler, Finite element analysis of the mechanical properties of cellular aluminium based on micro-computed tomography, Mater. Sci. Eng. A. (2011). doi:10.1016/j.msea.2011.02.031.

[50] T. Fiedler, M.A. Sulong, V. Mathier, I. V. Belova, C. Younger, G.E. Murch, Mechanical properties of aluminium foam derived from infiltration casting of salt dough, Comput. Mater. Sci. (2014). doi:10.1016/j.commatsci.2013.08.021.

[51] H. Mehboob, F. Tarlochan, A. Mehboob, S.H. Chang, Finite element modelling and characterization of 3D cellular microstructures for the design of a cementless biomimetic porous hip stem, Mater. Des. (2018). doi:10.1016/j.matdes.2018.04.002.

[52] L. Derpenski, A. Seweryn, Experimental Research into Fracture of EN-AW 2024 and EW-AW 2007 Aluminum Alloy Specimens with Notches Subjected to Tension, Exp. Mech. (2011). doi:10.1007/s11340-010-9420-9.

[53] M. Doroszko, A. Seweryn, Numerical modeling of the tensile deformation process of sintered 316L based on microtomography of porous mesostructures, Mater. Des. (2015). doi:10.1016/j.matdes.2015.09.006.

[54] MSC Software Corporation, Marc® 2014.2, Product Documentation, Volume B: Element Library, (2015).

[55] N. Otsu, THRESHOLD SELECTION METHOD FROM GRAY-LEVEL HISTOGRAMS., IEEE Trans Syst Man Cybern. (1979). doi:10.1109/tsmc.1979.4310076.

DECLARATION OF COMPETING INTERESTS

The authors declare that they have no known competing financial interests or personal relationships that could have appeared to influence the work reported in this paper.

ACKNOWLEDGEMENTS

The paper was accomplished under grant no. UMO-2016/23/N/ST8/03519 at the Bialystok University of Technology and financed by the National Science Centre (Poland).